Supporting Information

Alleviating competitive adsorption of hydrogen and hydroxyl intermediates on Ru by *d-p* orbital hybridization for hydrogen electrooxidation

Youkai Feng[1], Siguang Lu[1], Luhong Fu[2], Fulin Yang[1,*] and Ligang Feng[1,*]

[1] School of Chemistry and Chemical Engineering, Yangzhou University, Yangzhou, Jiangsu 225002, China

[2] College of Materials Science and Engineering, Huaqiao University, Xiamen, Fujian 361021, China

Corresponding authors' email addresses: yangfl@yzu.edu.cn;
ligang.feng@yzu.edu.cn

Experimental procedures

Chemical and materials. Ruthenium(III) chloride hydrate ($RuCl_3 \cdot nH_2O$, Aladdin Industrial, ≥ 99%), nickel(II) acetate tetrahydrate ($C_4H_6NiO_4 \cdot 4H_2O$, Aladdin Industrial, ≥ 99%), ethylene glycol ($C_2H_6O_2$, Aladdin Industrial, 98%), selenium (Se, Macklin Industrial, ≥ 99.999%), hydrazine hydrate ($N_2H_4 \cdot H_2O$, Sinopharm Chemical Reagent, ≥ 85%), ethanol anhydrous (C_2H_6O, Sinopharm Chemical Reagent, ≥ 99.7%), Vulcan XC-72R carbon black (size:50nm), potassium hydroxide (KOH, Aladdin Industrial, 99.99% metals basis, except sodium), isopropyl alcohol (C_3H_8O, Sinopharm Chemical Reagent, ≥ 99.5%), Nafion (Sigma-Aldrich, 5 wt. %). All solutions for synthesis and electrochemical tests were prepared by ultrapure water with a resistance of 18.2 MΩ (Thermo Fisher Scientific Co. LTD, USA).

Synthesis of $NiSe_2$. Dissolve 2 mmol nickel(II) acetate tetrahydrate and 8 mmol Se powder in a 150 mL beaker with 30 mL ultrapure water. Then add 30 mL 85% $N_2H_4 \cdot H_2O$ under consecutive stirring.[1] After mixing, transfer the mixture to a 100 mL stainless steel polytetrafluoroethylene lined autoclave and heat to 140 °C for 20 h. After cooling to room temperature, the synthesized $NiSe_2$ product was washed three times with anhydrous ethanol and ultrapure water, centrifuged, and finally dried under vacuum conditions at 60 °C for 10 hours.

Synthesis of Ru/$NiSe_2$/C-20. $RuCl_3$ solution (containing 20 mg Ru), $NiSe_2$ (20 mg), and ethylene glycol (40 mL) were added into a 250 mL three-necked flask and stirred to obtain a uniformly dispersed solution. The three-necked flask was placed in a microwave apparatus and radially heated under consecutive stirring and the power of 700 W, keeping at the temperature of 150 °C for 20 min.[2] After cooling to room temperature, the three-necked flask was taken out. 30 mg Vulcan XC-72 carbon blacks were added to the solution and kept stirring for another 30 min. The samples were then separated by centrifugation for 4 times, during which the samples were ultrasonically cleaned twice with ultrapure water and absolute ethanol, and once with absolute ethanol. Finally, the as-prepared Ru/$NiSe_2$/C-20 sample could be obtained after drying under a vacuum for 10 h at 60 °C. Other samples with different contents

of $NiSe_2$ could be obtained by varying the feeding ratio of Ni and Ru (0.5, 1.5, 4) at a constant addition of Ru^{3+} (20 mg). And the mass of Vulcan XC-72 carbon blacks was tapered off to keep the same total weight of 100 mg (Ru + $NiSe_2$ + C) The samples were named Ru/$NiSe_2$/C-10, Ru/$NiSe_2$/C-30, and Ru/$NiSe_2$, respectively, corresponding to the feeding ratios of Ni and Ru (0.5, 1.5, 4). Ru/C was synthesized in a similar method without the addition of $NiSe_2$.

Materials characterization.

Powder X-ray diffraction (XRD) patterns were recorded on a Bruker D8 Advance powder X-ray diffractometer using a Cu Kα (λ = 1.5405 Å) radiation source operating at 40 kV and 30 mA at a scanning rate of 5° min^{-1}. The Zeiss Supra55 field emission scanning electron microscope (SEM) was performed to obtain the SEM images. The high-resolution transmission electron microscopy (HRTEM) was performed on FEI Tecnai G2 F30 STWIN (USA) equipped with the energy-dispersive X-ray spectrum module to visualize the morphologies and element distribution of the samples. High-angle annular dark-field scanning TEM (HAADF-STEM) images were acquired by using JEMARM300F GRAND ARM (JEOL, Japan) with an acceleration voltage of 300kV. Surface analysis of the sample was studied by X-ray photoelectron spectroscopy (XPS, Thermo Science, ESCALAB 250Xi, USA). Inductively coupled plasma atomic emission spectroscopy (ICP-AES) analysis was performed on Optima 7300 DV.

Preparation of working electrodes.

Before the HOR tests, 5.0 mg Ru/C, Ru/$NiSe_2$/-10, Ru/$NiSe_2$/C-20, Ru/$NiSe_2$/C-30, and Ru/$NiSe_2$ were mixed with 1.0 mL of isopropanol solvent containing 0.05 wt. % Nafion, and then ultrasonicated for 30 min to form the homogeneous inks, respectively. The glassy carbon (GC) electrode with a diameter of 5 mm was polished with a 50 nm gamma alumina powder slurry and ultrasonically cleaned three times with ultrapure water and ethanol in sequence to obtain a smooth and clean surface. After drying naturally in air, 6.0 μL of ink was cast dropwise on the surface and dried

in the air for electrochemical tests. The loadings of Ru on electrocatalysts-decorated electrodes could be calculated from the ICP-AES data, as listed in Table S1.

Electrochemical measurements

Electrochemical tests were conducted at GAMRY Reference 3000 electrochemistry workstation in a standard three-electrode system with the electrocatalyst-decorated GC electrode serving as the working electrode, and the graphite rod (diameter of 1 cm) serving as the counter electrode as well as the Hg/HgO electrode (fully filled with 0.1 M KOH for the tests in pH 13 solutions or 1.0 M KOH for the tests in pH 14 solutions) served as reference electrode. In electrochemical tests, all operations were performed at a constant temperature of 298 ± 1 K. All the measured potentials were referred to the reversible hydrogen electrode (RHE) potential with *iR*-compensated.

Before HOR evaluation, we stabilized the GC disk surface at open circuit potential for more than 300 s in H_2-saturated 0.1 M or 1.0 M KOH solutions, which was getting closer to the hydrogen equilibrium potential. Then, the HOR polarization curves were drawn at a scan rate of 5 mV s^{-1} at an RDE rotation rate of 1600 rpm and a potential range between −0.08 and 0.62 V vs RHE for Ru/C, Ru/$NiSe_2$/C-10, Ru/$NiSe_2$/C-20, Ru/$NiSe_2$/C-30, and Ru/$NiSe_2$ samples. For the accelerated durability testing (ADT), Ru/$NiSe_2$/C-20 was cycled for 1000 CVs at a scan rate of 200 mV s^{-1} with potentials ranging from −0.08 to 0.62V vs RHE in an N_2-saturated electrolyte of 0.1 M KOH. Then the HOR polarization curves were obtained at the H_2-saturated 0.1 M KOH to evaluate the stability.

In the CO-stripping tests, the electrode potential was maintained at 0.1 V vs RHE for 15 min in 0.1 M KOH solution saturated by 99.99 % CO to allow CO adsorb on the metal surface, followed by N_2 purgation for another 15 min to remove residual CO from the electrolyte. The CO stripping current was obtained through CV at a sweep rate of 20 mV s^{-1} in the 0.02 to 0.92 V vs RHE potential range.

In the high-potential oxidation experiment, the GC electrode modified with Ru/$NiSe_2$/C-20 was used to obtain Ru/$Ni(OH)_2$/C-20 at a scan rate of 50 mV s^{-1}

during the potential range of −0.08 to 1.22 V vs RHE under H_2-saturated 0.1 M KOH solution. Subsequently, the HOR polarization curve of Ru/Ni(OH)$_2$/C-20 was obtained at a potential range of −0.08 to 0.62 V vs RHE.

The electrochemical impedance spectroscopy (EIS) test was carried out under the conditions of AC impedance spectrum ranging from 100 kHz to 1 Hz and voltage disturbance of 5 mV. The real part of the resistance at 1 kHz is taken as the uncompensated resistance (R_u),[3] and the *iR*-free potential ($E_{iR\text{-free}}$) is obtained according to the following equation (Eq. S1),

$$E_{iR-free} = E - iR_u \quad \text{Eq.S1}$$

The measured current density (j), diffusion current density (j^d), and kinetic current density (j^k) can be related by the Koutecky-Levich equation (Eq. S2, Eq. S3),

$$\frac{1}{j} = \frac{1}{j^k} + \frac{1}{j_d} \quad \text{Eq.S2}$$

$$j_d = 0.62nFD^{2/3}v^{-1/6}c_0\omega^{1/2} = Bc_0\omega^{1/2} \quad \text{Eq.S3}$$

Where n is the number of electrons involved in the oxidation reaction (2), F is the Faraday constant (96485 C mol^{-1}), D is the diffusion coefficient of the reactant (3.7 × 10^{-5} cm^2 s^{-1}), v is the viscosity of the electrolyte (1.01 × 10^{-2} cm^2 s^{-1}), c_0 is the solubility of H_2 in the electrolyte (7.33 × 10^{-4} mol L^{-1}), ω is the rotational speed, and B is the Levich constant.

The exchange current density (j^0) and the kinetic current density j^k are related by the Butler-Volmer equation (Eq. S4),

$$j^k = j^0[e^{\frac{\alpha F}{RT}\eta} - e^{\frac{-(1-\alpha)F}{RT}\eta}] \quad \text{Eq.S4}$$

j^0 could be also obtained from the approximate Butler-Volmer equation (Eq. S5),

$$j = j^0\frac{\eta F}{RT} \quad \text{Eq.S5}$$

Where, α, η, R, and T represent the transfer coefficient, overpotential, universal gas constant (8.314 J mol^{-1} K^{-1}), and Kelvin temperature, respectively.

DFT calculations

DFT calculations were performed using the CASTEP module in the Materials Studio program at Bio Accelrys. The generalized gradient approximation method (GGA) with the Perdew-Burke-Ernzerh (PBE) functional was used to describe the exchange and correlation interactions.[4, 5] The interactions between valence electrons and ionic cores were described by Ultrasoft pseudo-potential. A two-layer √3 × √3 supercell of cubic $NiSe_2$(111) slabs, a one-layer 6 × 6 supercell of graphene(001), and a one-layer 4 × 4 supercell of $Ni(OH)_2$ were constructed to simulate the $NiSe_2$, carbon, and $Ni(OH)_2$ supports, respectively. In $Ni(OH)_2$, three H toms were deleted for anchoring the Ru cluster. A Ru cluster with 13 atoms was chosen to mimic the supported Ru nanocrystals, which could reflect the *hcp* phase, consistent with the experimental results. For each model, the vacuum gap was set as 15 Å. And the atoms on the bottom layer were fixed, and the other atoms were fully optimized. The electronic wave functions were expanded on a plane wave basis with a cut-off energy of 350 eV. And 2 × 2 × 1 Monkhorst-Pack grid k-points were employed for the geometric optimizations. The convergence threshold is set as 1.0^{-6} eV in energy and 0.03 eV/Å in force, respectively. The adsorption free energies of each intermediate including H_{ad}, OH_{ad}, H_{ad}+OH_{ad}, and H_2O_{ad} were determined by the following formula $\Delta G = \Delta E + \Delta ZPE - T\Delta S$, where ΔE, ΔZPE, and ΔS represent the binding energy, zero-point energy change and entropy change of the adsorption process, respectively.[6, 7] Different sites have been considered.

Results and Discussion

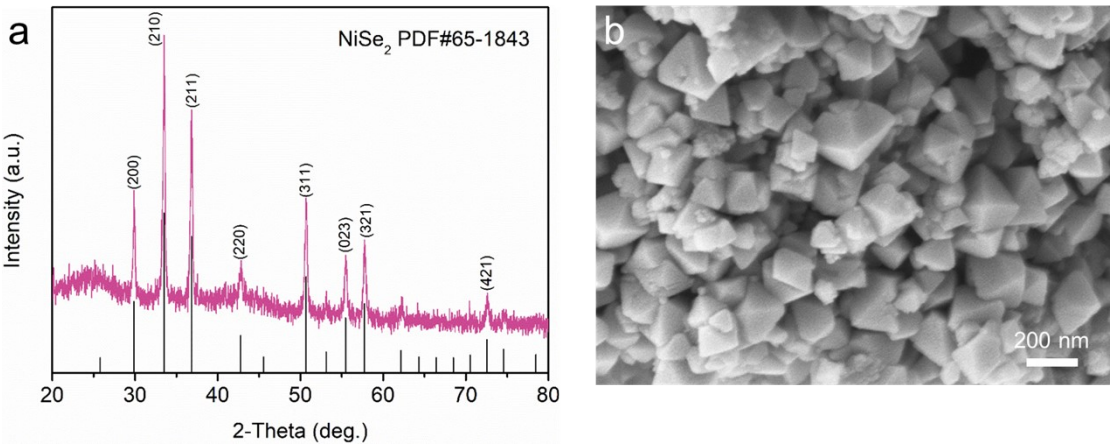

Figure S1. (a) XRD pattern and (b) SEM image of $NiSe_2$.

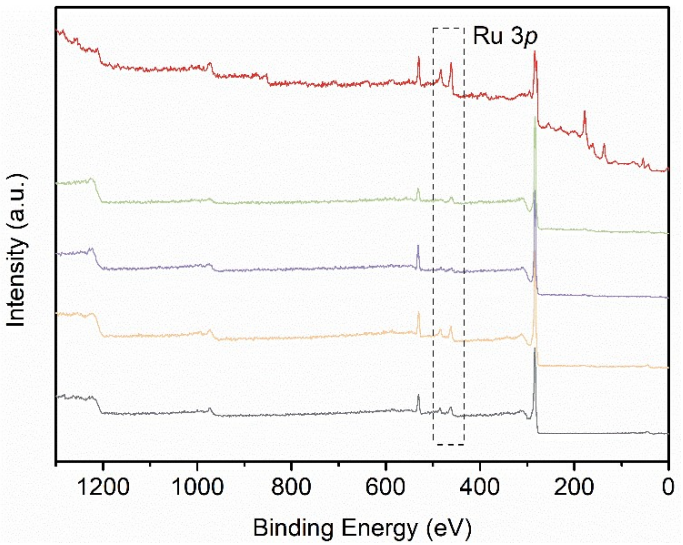

Figure S2. The XPS survey spectra of Ru/C, Ru/$NiSe_2$/C-10, Ru/$NiSe_2$/C-20, Ru/$NiSe_2$/C-30, and Ru/$NiSe_2$.

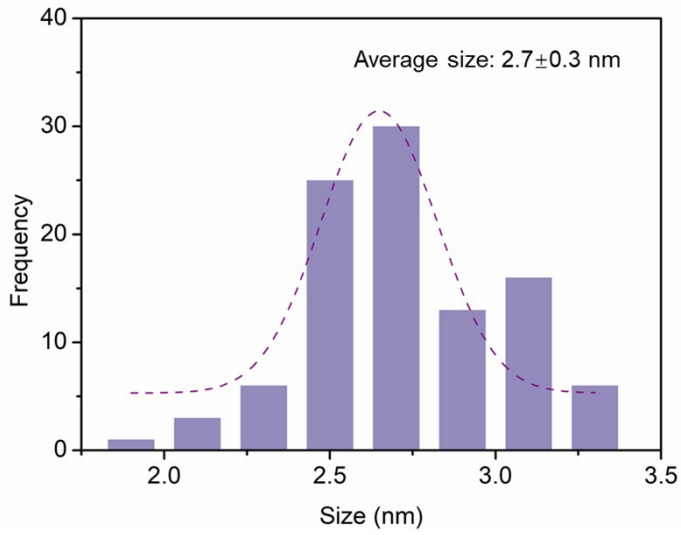

Figure S3. Size distribution histograms of $Ru/NiSe_2/C$-20.

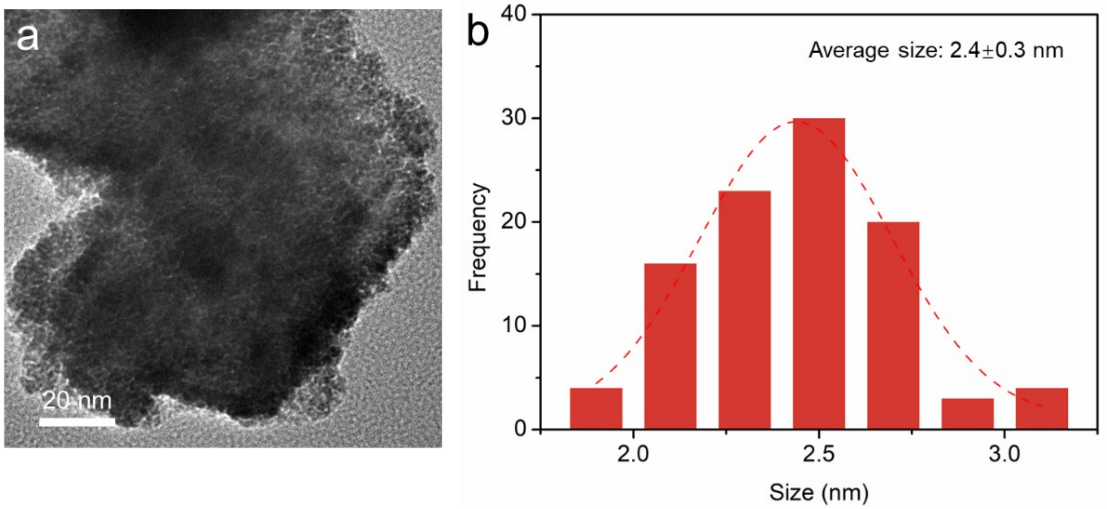

Figure S4. (a) HRTEM image and (b) size distribution histograms of Ru/$NiSe_2$.

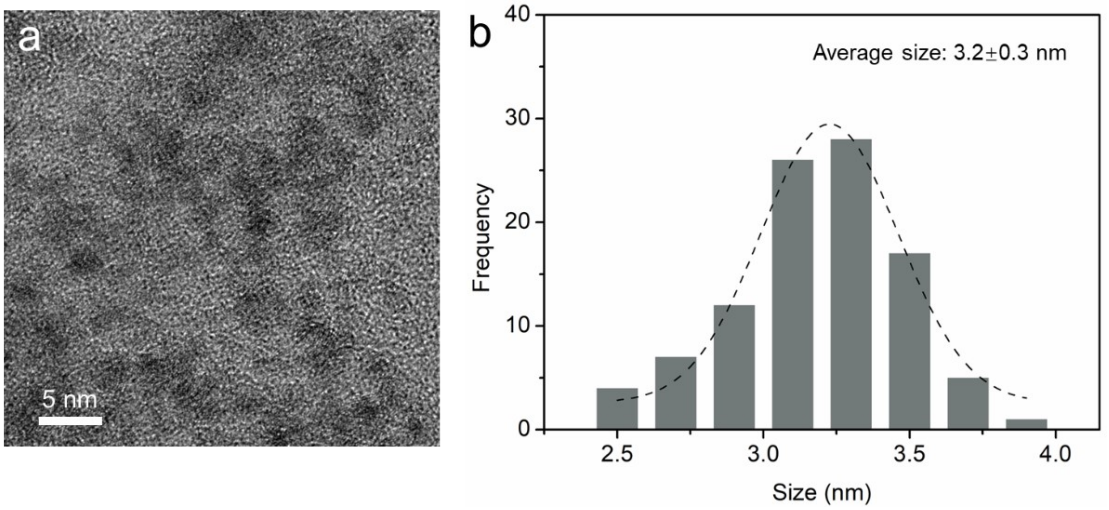

Figure S5. (a) HRTEM image and (b) size distribution histograms of Ru/C.

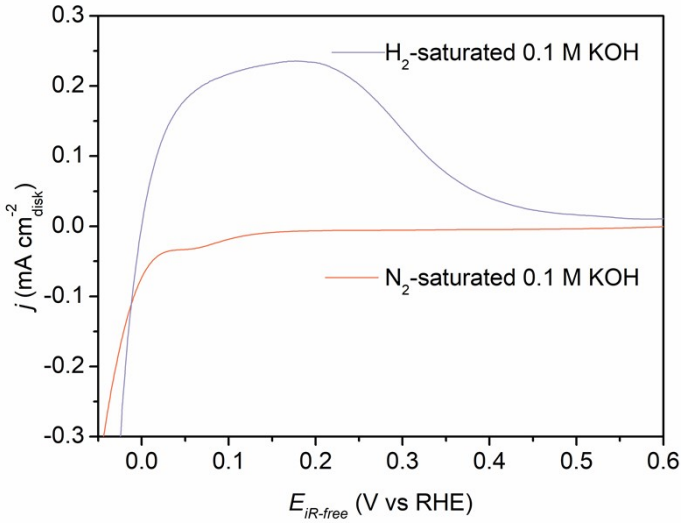

Figure S6. Polarization curves of $Ru/NiSe_2/C$-20 in H_2 or N_2-saturated 0.1 M KOH electrolytes.

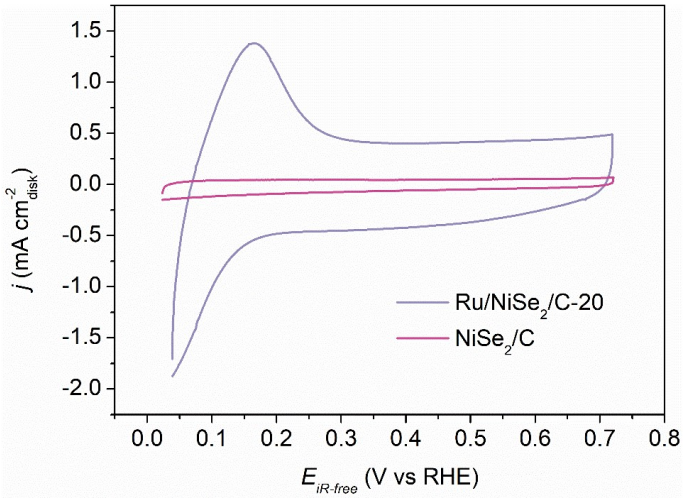

Figure S7. CVs in N_2-saturated 0.1 M KOH at a scan rate of 50 mVs^{-1} for $Ru/NiSe_2/C$-20 and $NiSe_2/C$.

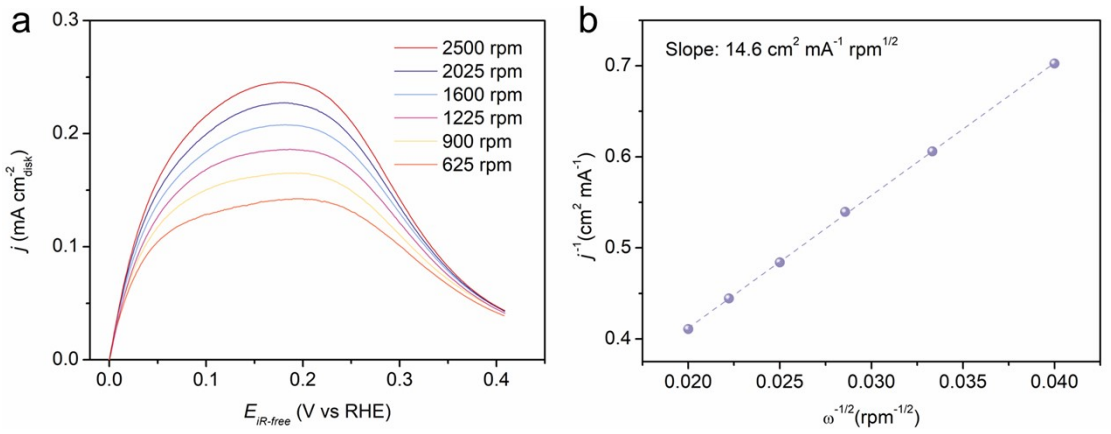

Figure S8. (a) HOR polarization curves in H_2-saturated 0.1 M KOH with the scanning rate of 5 mV s^{-1} at the rotating rates ranging from 2500 to 625 rpm of $Ru/NiSe_2/C$-20 and (b) corresponding Koutecky-Levich plot.

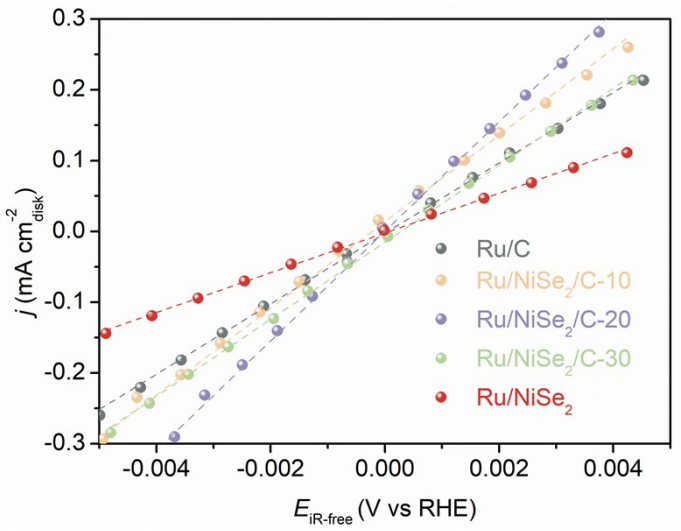

Figure S9. Linear fitting curves in the micro-polarization region.

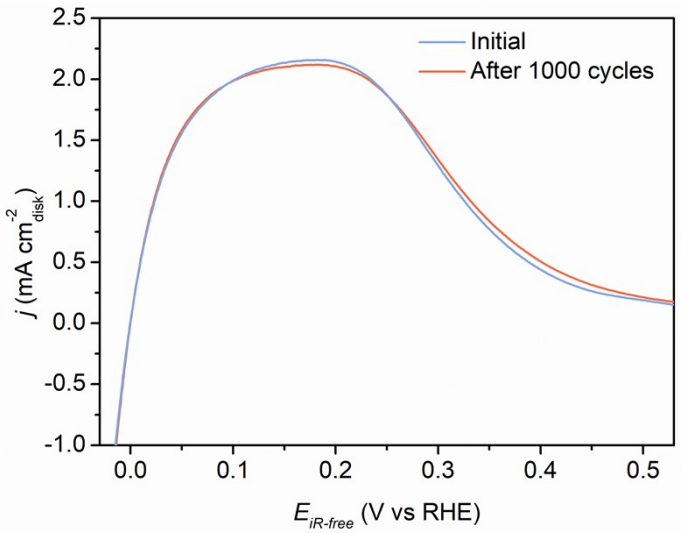

Figure S10. HOR polarization curves of $Ru/NiSe_2/C$-20 recorded before and after 1000 cycles in 0.1 M KOH (ADT).

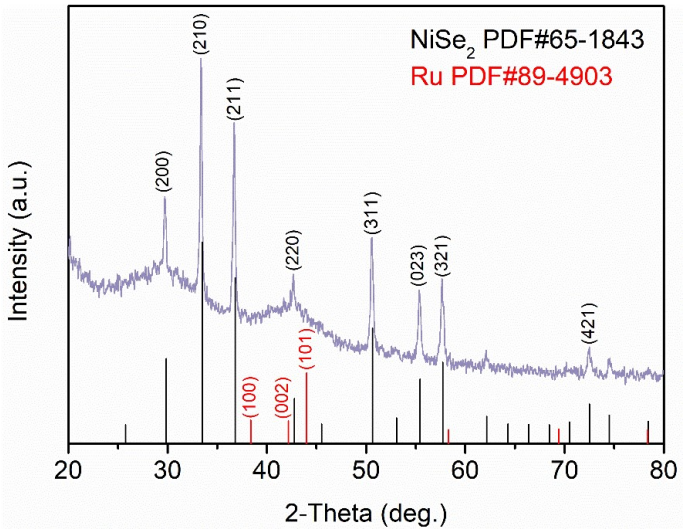

Figure S11. XRD pattern Ru/$NiSe_2$/C-20 after ADT.

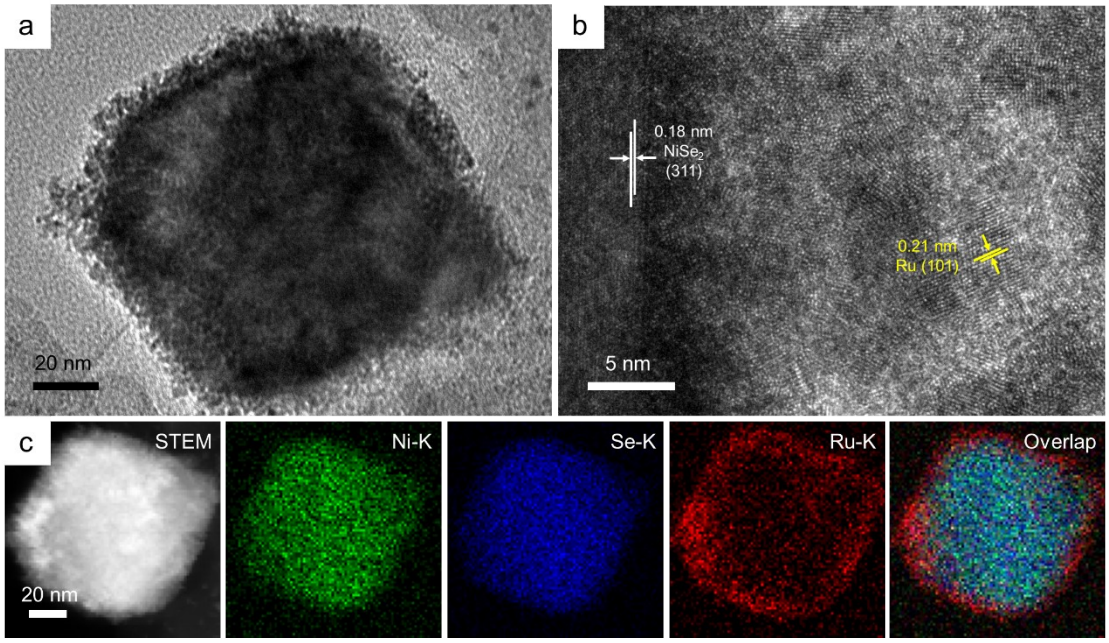

Figure S12. (a) TEM image, (b) HRTEM image, and (c) corresponding EDS mapping images of $Ru/NiSe_2/C$-20 after ADT.

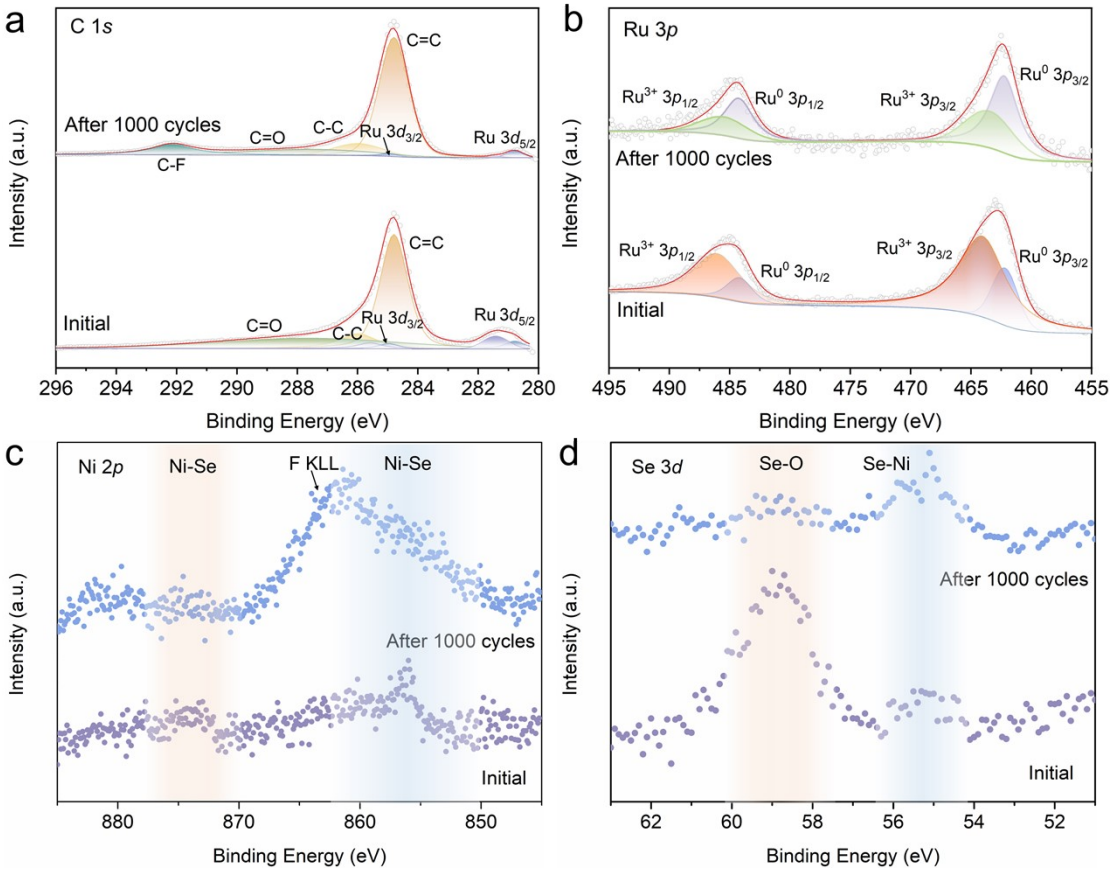

Figure S13. High-resolution XPS spectra of (a) C 1*s*, (b) Ru 3*p*, (c) Ni 2*p*, and (d) Se 3*d* for Ru/$NiSe_2$/C-20 before and after 1000 CV cycles.

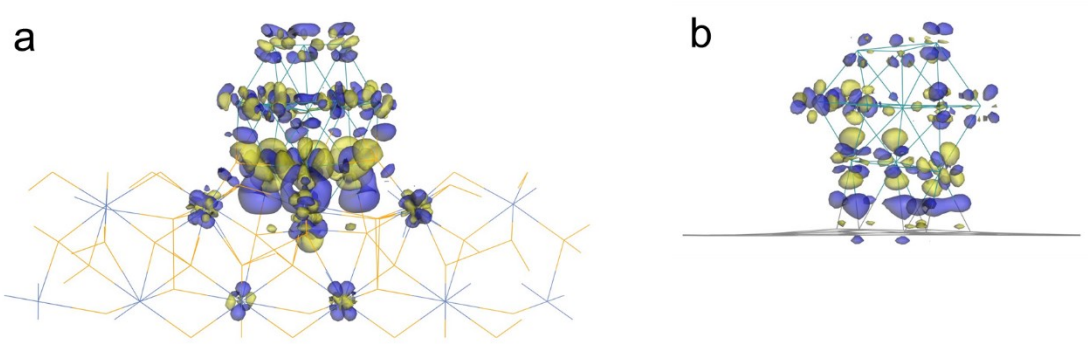

Figure S14. Charge density difference plots of (a) Ru/$NiSe_2$ and (b) Ru/C with the isosurface value of 0.05 $eÅ^{-3}$. The yellow and blue outlines show electron accumulation and depletion, respectively.

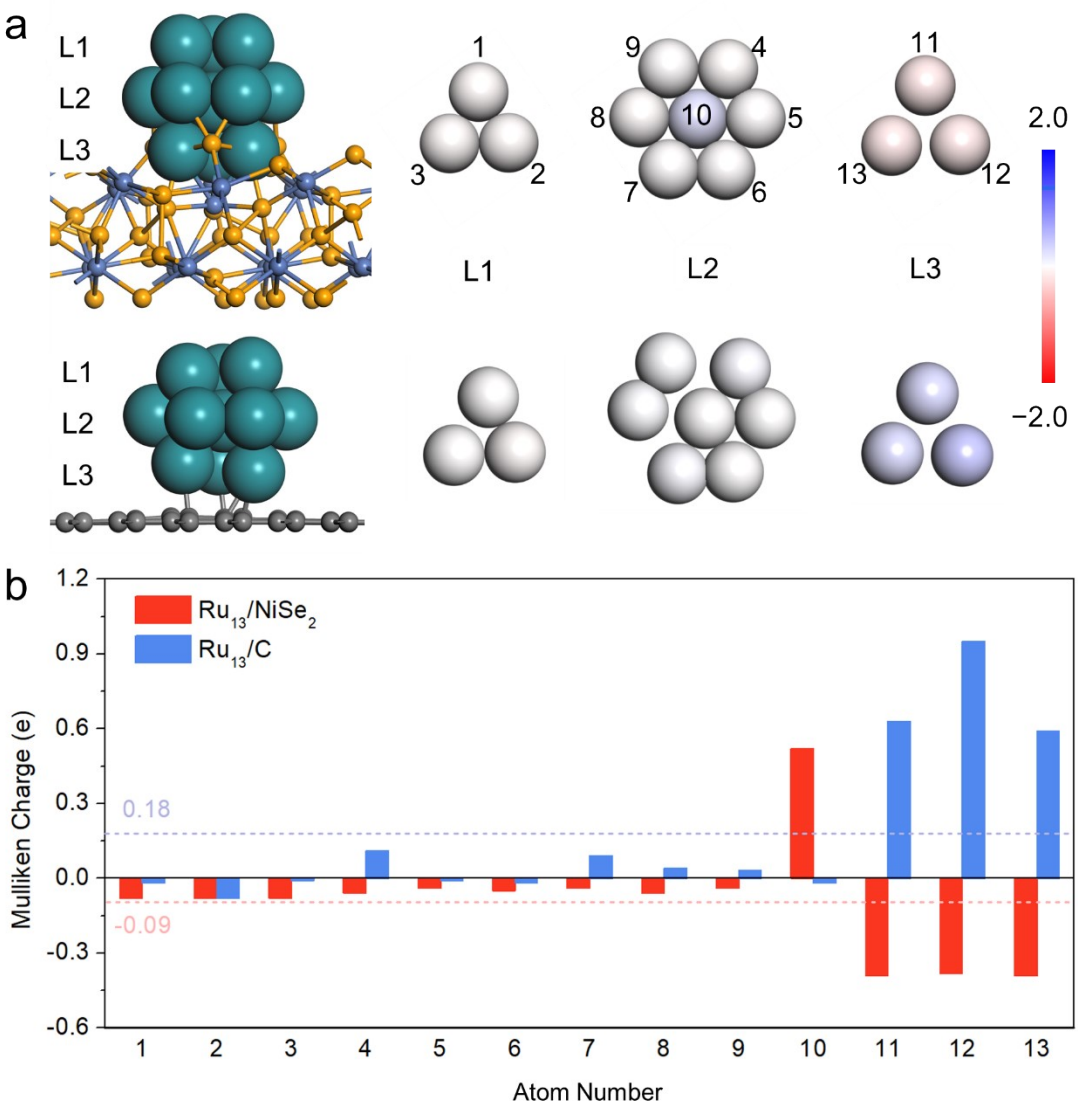

Figure S15. (a) Mulliken charge distribution plot of each atom on $NiSe_2$(111) or C(001) supported Ru_{13} clusters and (b) the corresponding charge values statics. The dash lines indicate the average values of $Ru/NiSe_2$ and Ru/C.

a

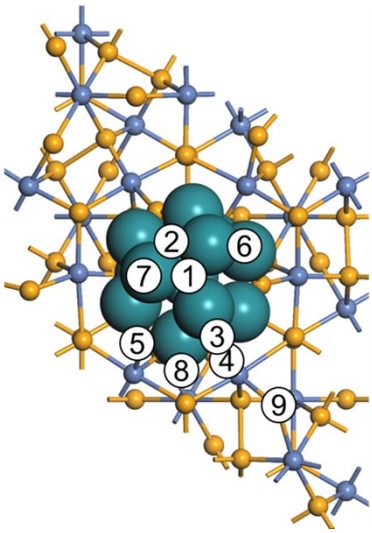

b

Site	Type	ΔG_H/eV	ΔG_{OH}/eV
1	hollow	unstable (2)	unstable (2)
2	bridge	−0.21	−0.50
3	hollow	unstable (4)	−0.69
4	bridge	−0.54	−0.27
5	bridge	−0.20	−0.28
6	bridge	−0.34	−0.43
7	top	unstable (2)	−0.76
8	top	unstable (4)	unstable (5)
9	$NiSe_2$	unstable (4)	0.67

Figure S16. (a) Different adsorption sites for H_{ad} and OH_{ad} on the Ru/$NiSe_2$ model. (b) Corresponding free energy values. (The numbers in parentheses represent the final stable sites).

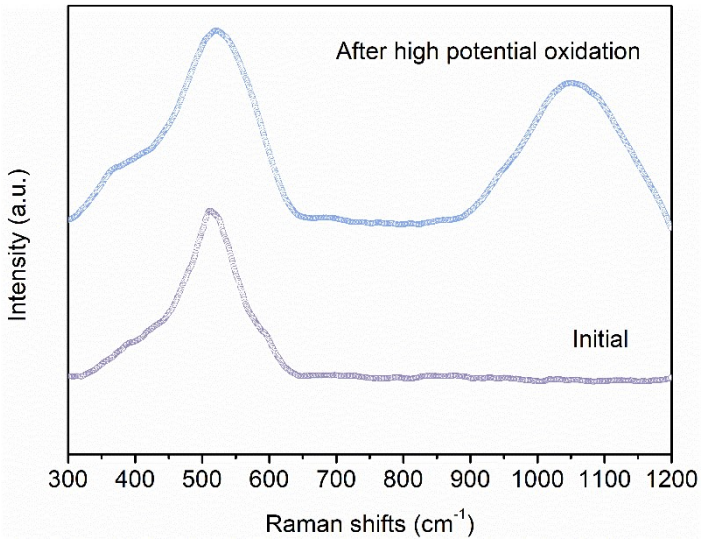

Figure S17. Raman spectra of $NiSe_2$ before and after high-potential oxidation.

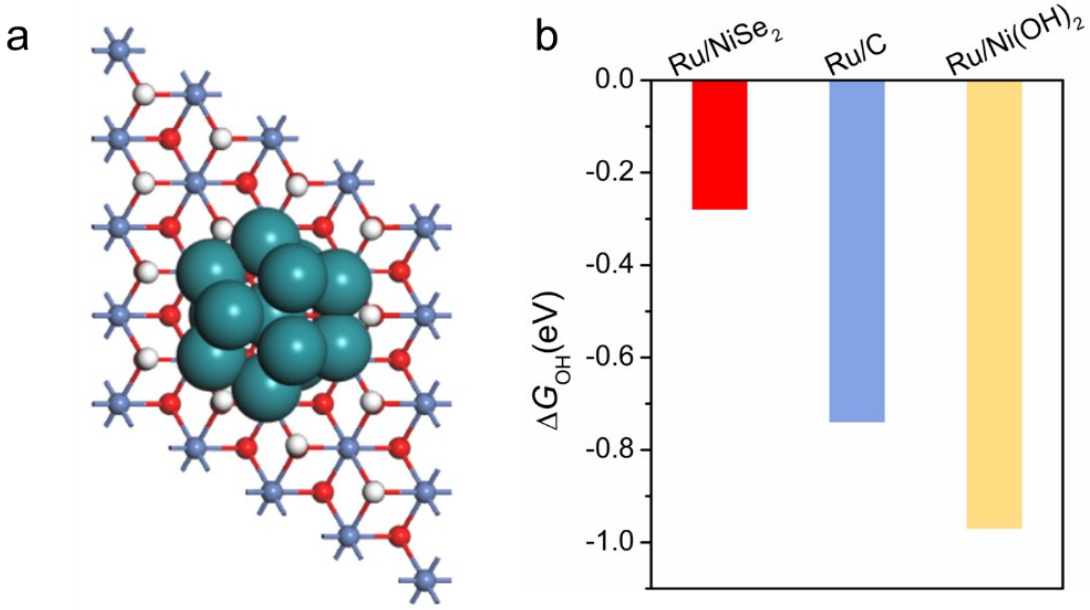

Figure S18. (a) Model of Ru/Ni(OH)$_2$ and (b) the comparison of the ΔG_{OH} values between Ru/NiSe$_2$, Ru/C, and Ru/Ni(OH)$_2$.

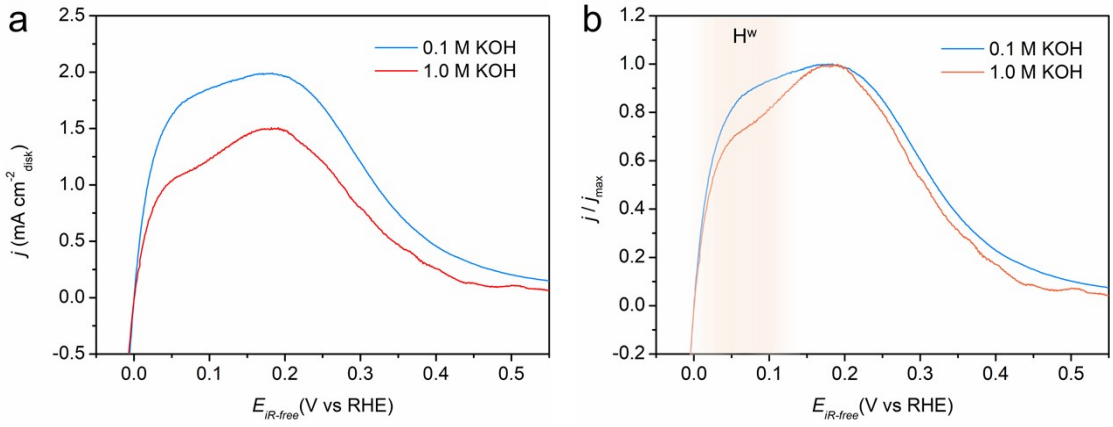

Figure S19. (a) HOR polarization curves and (b) Normalized HOR polarizations of $Ru/NiSe_2/C$-20 in 0.1 M and 1.0 M KOH solutions.

Table S1. Ru, Ni, and Se atomic percentages for four samples of $Ru/NiSe_2/C$-X (X = 10, 20, 30) and $Ru/NiSe_2$.

Sample	Atomic percentage (%)			Ru/Ni atomic ratio
	Ru	Ni	Se	
$Ru/NiSe_2/C$-10	52.63	19.30	28.07	2.73
$Ru/NiSe_2/C$-20	41.82	22.09	36.09	1.89
$Ru/NiSe_2/C$-30	32.71	25.13	42.15	1.30
$Ru/NiSe_2$	14.67	31.37	53.96	0.47

Table S2. The data of HOR activities in this work obtained by Butler-Volmer fitting and linear fitting.

Sample	Butler-Volmer fitting				Linear fitting	
	Loading (μg_{Ru} cm_{disk}^{-2})	$j^{0,s}$ (mA cm_{ECSA}^{-2})	$j^{0,m}$ (mA μg_{Ru}^{-1})	$j^{k,m}$@50mV (mA μg_{Ru}^{-1})	$j^{0,s}$ (mA cm_{ECSA}^{-2})	$j^{0,m}$ (mA μg_{Ru}^{-1})
Ru/C	3.60	0.030	0.442	0.967	0.025	0.365
Ru/$NiSe_2$/C-10	3.48	0.067	0.663	1.896	0.053	0.525
Ru/$NiSe_2$/C-20	2.43	0.111	0.882	2.510	0.084	0.670
Ru/$NiSe_2$/C-30	2.86	0.115	0.555	1.796	0.085	0.411
Ru/$NiSe_2$	8.84	0.560	0.107	0.321	0.372	0.063

Table S3. Comparison of the HOR activity in 0.1 M KOH referring to Ru-based catalysts.

Catalyst	Loading (μg_{Ru} cm_{disk}^{-2})	$j^{0,s}$ (mA cm_{ECSA}^{-2})	$j^{0,m}$ (mA μg_{Ru}^{-1})	$j^{k,m}$@50mV (mA μg_{Ru}^{-1})	Reference
$Ru/NiSe_2$/C-20	2.43	0.111	0.882	2.510	This work
$Ru/NiSe_2$	8.84	0.560	0.107	0.321	
Ru/C	3.60	0.030	0.442	0.967	
Ru-SO_4	4.78	0.548	0.462	1.182	8
Ru/C	4.65		0.231		
Ru-Ru_2P/C	8.33		0.375	1.265	
Ru_2P/C	9.26		0.252	0.558	9
Ru/C	9.54		0.157	0.228	
Ru_7Ni_3/C	3.87				10
Ru/C	3.87				
Mo-Ru-NSAs				2.45	11
Sn-Ru/C	6.26	0.47		1.79	12
Ga-Ru/C	7.04	0.3		0.593	
Ru/C	7.8	0.24		0.274	
Ru@C-280		0.49		9.53	13
Ru@C-340		0.39		1.2	
Ru@C-400		0.31		0.64	
Ru/C		0.23		0.19	
Mo-Ru-1/C	5.97	0.3		1.73	14
Mo-Ru-2/C	5.92	0.35		1.86	
Mo-Ru-3/C	5.6	0.23		1.25	
Ru/C	6.5	0.14		0.24	
P-Ru-1/C	1.22	0.25	0.12		15

P-Ru-2/C	1.12	0.35	0.19		
P-Ru-3/C	6.06	0.72	0.43		
P-Ru-4/C	1.28	0.66	0.36		
P-Ru-5/C	1.21	0.63	0.26		
Ru/C		0.15	0.13		
Ru/C				0.052	16
IO-Ru-TiO_2/C				0.907	
MoO_X-Ru fcc			1.66	5.72	
MoO_X-Ru hcp			0.61	1.16	17
Ru/C			0.089	0.13	
Ru/C	10			0.23	18
RuNi/C	10			2.34	

Table S4. XPS peak data about the C 1*s* spectra of $Ru/NiSe_2/C$-20 before and after ADT.

Catalysts	Peak	Binding energy (eV)	Content
$Ru/NiSe_2/C$-20	C=C	284.8	49.75%
	C=O	287.6	11.15 %
	C–C	287.6	26.66 %
$Ru/NiSe_2/C$-20 after ADT	C=C	284.8	63.02 %
	C=O	287.6	9.52 %
	C–C	286.0	12.48 %
	C–F	292.1	11.21 %

Table S5. XPS peak data about the Ru 3*p* spectra of $Ru/NiSe_2/C$-20 before and after ADT.

Catalysts	Ru $3p_{3/2}$		Ru $3p_{1/2}$		Content	Ru^0/Ru^{3+}
	Peak	Binding energy (eV)	Peak	Binding energy (eV)		
$Ru/NiSe_2/C$-20	Ru^0	462.1	Ru^0	484.1	22.81 %	0.30
	Ru^{3+}	464.3	Ru^{3+}	486.3	77.19 %	
$Ru/NiSe_2/C$-20 after ADT	Ru^0	462.1	Ru^0	484.1	67.38 %	2.35
	Ru^{3+}	464.3	Ru^{3+}	486.3	28.62 %	

Table S6. XPS peak data about the Ni 2*p* spectra of $Ru/NiSe_2/C$-20 before and after ADT.

Catalysts	Ni 2*p*			
	Peak	Binding energy (eV)	Peak	Binding energy (eV)
$Ru/NiSe_2/C$-20	Ni–Se	856.2	Ni–Se	873.3
$Ru/NiSe_2/C$-20 after ADT	Ni–Se	856.1	Ni–Se	873.2

Table S7. XPS peak data about the Se 3*d* spectra of Ru/$NiSe_2$/C-20 before and after ADT.

Catalysts	Se 3*d*			
	Peak	**Binding energy (eV)**	**Peak**	**Binding energy (eV)**
Ru/$NiSe_2$/C-20	Se–Ni	55.1	Se–O	58.8
Ru/$NiSe_2$/C-20 after ADT	Se–Ni	55.0		

Table S8. Mulliken charge (e^-) of each Ru atoms in $Ru/NiSe_2$ and Ru/C, corresponding to Figure S12.

Atom No.	$Ru/NiSe_2$	Ru/C
1	−0.08	−0.02
2	−0.08	−0.08
3	−0.08	−0.01
4	−0.06	0.11
5	−0.04	−0.01
6	−0.05	−0.02
7	−0.04	0.09
8	−0.06	0.04
9	−0.04	0.03
10	0.52	−0.02
11	−0.39	0.63
12	−0.38	0.95
13	−0.39	0.59

References

(1) Zhu, S.; Li, Q.; Wei, Q.; Sun, R.; Liu, X.; An, Q.; Mai, L., $NiSe_2$ Nanooctahedra as an Anode Material for High-Rate and Long-Life Sodium-Ion Battery. *ACS Appl. Mater. Interfaces* **2017,** *9*, 311-316.

(2) Harpeness, R.; Peng, Z.; Liu, X.; Pol, V. G.; Koltypin, Y.; Gedanken, A., Controlling the agglomeration of anisotropic Ru nanoparticles by the microwave–polyol process. *J. Colloid Interf. Sci.* **2005,** *287*, 678-684.

(3) Sheng, W.; Gasteiger, H. A.; Shao-Horn, Y., Hydrogen Oxidation and Evolution Reaction Kinetics on Platinum: Acid vs Alkaline Electrolytes. *J. Electrochem. Soc.* **2010,** *157*, B1529.

(4) Vanderbilt, D., Soft self-consistent pseudopotentials in a generalized eigenvalue formalism. *Phys. Rev. B* **1990,** *41*, 7892-7895.

(5) Perdew, J. P.; Burke, K.; Ernzerhof, M., Generalized Gradient Approximation Made Simple. *Phys. Rev. Lett.* **1996,** *77*, 3865-3868.

(6) Ferrin, P.; Nilekar, A. U.; Greeley, J.; Mavrikakis, M.; Rossmeisl, J., Reactivity descriptors for direct methanol fuel cell anode catalysts. *Surf Sci* **2008,** *602*, 3424-3431.

(7) Nørskov, J. K.; Bligaard, T.; Logadottir, A.; Kitchin, J. R.; Chen, J. G.; Pandelov, S.; Stimming, U., Trends in the Exchange Current for Hydrogen Evolution. *J. Electrochem. Soc.* **2005,** *152*, J23.

(8) Yang, C.; Li, Y.; Yue, J.; Cong, H.; Luo, W., Promoting water formation in sulphate-functionalized Ru for efficient hydrogen oxidation reaction under alkaline electrolytes. *Chem. Sci.* **2023,** *14*, 6289-6294.

(9) Su, L.; Jin, Y.; Gong, D.; Ge, X.; Zhang, W.; Fan, X.; Luo, W., The Role of Discrepant Reactive Intermediates on Ru-Ru2P Heterostructure for pH-Universal

Hydrogen Oxidation Reaction. *Angew. Chem. Int. Edit.* **2023,** *62*, e202215585.

(10) Xue, Y.; Shi, L.; Liu, X.; Fang, J.; Wang, X.; Setzler, B. P.; Zhu, W.; Yan, Y.; Zhuang, Z., A highly-active, stable and low-cost platinum-free anode catalyst based on RuNi for hydroxide exchange membrane fuel cells. *Nat. Commun.* **2020,** *11*, 5651.

(11) Li, L.; Liu, S.; Zhan, C.; Wen, Y.; Sun, Z.; Han, J.; Chan, T.-S.; Zhang, Q.; Hu, Z.; Huang, X., Surface and lattice engineered ruthenium superstructures towards high-performance bifunctional hydrogen catalysis. *Energy Environ. Sci.* **2023,** *16*, 157-166.

(12) Wu, L.; Su, L.; Liang, Q.; Zhang, W.; Men, Y.; Luo, W., Boosting Hydrogen Oxidation Kinetics by Promoting Interfacial Water Adsorption on d-p Hybridized Ru Catalysts. *ACS Catal.* **2023,** *13*, 4127-4133.

(13) Yang, Z.; Lai, W.; He, B.; Wang, J.; Yu, F.; Liu, Q.; Liu, M.; Zhang, S.; Ding, W.; Lin, Z.; Huang, H., Tailoring Interfacial Chemistry of Defective Carbon-Supported Ru Catalyst Toward Efficient and CO-Tolerant Alkaline Hydrogen Oxidation Reaction. *Adv. Energy Mater.* **2023,** *13*, 2300881.

(14) Zhao, Y.; Wu, D.; Luo, W., Correlating Alkaline Hydrogen Electrocatalysis and Hydroxide Binding Energies on Mo-Modified Ru Catalysts. *ACS Sustain. Chem. Eng.* **2022,** *10*, 1616-1623.

(15) Zhao, Y.; Wang, X.; Cheng, G.; Luo, W., Phosphorus-Induced Activation of Ruthenium for Boosting Hydrogen Oxidation and Evolution Electrocatalysis. *ACS Catal.* **2020,** *10*, 11751-11757.

(16) Jiang, J.; Tao, S.; He, Q.; Wang, J.; Zhou, Y.; Xie, Z.; Ding, W.; Wei, Z., Interphase-oxidized ruthenium metal with half-filled d-orbitals for hydrogen oxidation in an alkaline solution. *J. Mater. Chem. A* **2020,** *8*, 10168-10174.

(17) Li, L.; Liu, C.; Liu, S.; Wang, J.; Han, J.; Chan, T.-S.; Li, Y.; Hu, Z.; Shao, Q.; Zhang, Q.; Huang, X., Phase Engineering of a Ruthenium Nanostructure toward High-Performance Bifunctional Hydrogen Catalysis. *ACS Nano* **2022,** *16*, 14885-14894.

(18) Jiang, T.; Liu, Z.; Yuan, Y.; Zheng, X.; Park, S.; Wei, S.; Li, L.; Ma, Y.; Liu, S.; Chen, J.; Zhu, Z.; Meng, Y.; Li, K.; Sun, J.; Peng, Q.; Chen, W., Ultrafast Electrical Pulse Synthesis of Highly Active Electrocatalysts for Beyond-Industrial-Level Hydrogen Gas Batteries. *Adv. Mater.* **2023**, *35,* 2300502.